



Research article

Robust QRS detection based on simulated degenerate optical parametric oscillator-assisted neural network

Zhiqiang Liao ^{a,b,1}, Zhuozheng Shi ^{b,c,*}, Md Shamim Sarker ^{a,b}, Hitoshi Tabata ^{a,b,**}

^a Department of Electrical Engineering and Information Systems, Graduate School of Engineering, The University of Tokyo, Tokyo, 113-8656, Japan

^b Department of Bioengineering, Graduate School of Engineering, The University of Tokyo, Tokyo, 113-8656, Japan

^c Bioinformatics Interdepartmental Program, University of California Los Angeles, Los Angeles, CA, USA

ARTICLE INFO

Keywords:

Electrocardiogram
QRS-Wave detection
Simulated degeneration unit
Degenerate optical parametric oscillator
Convolutional neural network

ABSTRACT

Accurately detecting the depolarization QRS complex in the ventricles is a fundamental requirement for cardiovascular disease detection using electrocardiography (ECG). In contrast to traditional signal enhancement algorithms, emerging neural network approaches have shown promise for QRS detection because of their generalizability on complex data. However, the inevitable noise present during ECG recording leads to a decrease in the performance of neural networks. To enhance the robustness and performance of neural network-based QRS detectors, we propose a simulated degeneration unit (SDU)-assisted convolutional neural network (CNN). An SDU simulates the physical degeneration process of interfering optical pulses, which can effectively suppress in-band noise. Through comprehensive performance evaluations on three open-source databases, the SDU-enhanced CNN-based approach demonstrated better performance in detecting QRS complexes than other recently reported QRS detectors. Furthermore, real-world noise injection tests indicate that the optimal noise robustness boundary for the CNN equipped with SDU is 167–300% higher than that for the CNN without SDU.

1. Introduction

The electrocardiogram (ECG) is a fundamental diagnostic tool used in medicine to monitor and evaluate the electrical activity of the heart [1–3]. It records the electrical impulses generated by the heart during each heartbeat cycle. ECGs are non-invasive and involve the placement of electrodes on the body surface to measure electrical signals, providing crucial insights into cardiac health. Among the various components captured in an ECG, the QRS complex is of paramount importance because it represents a specific electrical event within the cardiac cycle, i.e., ventricular depolarization. The QRS complex can be used to analyze cardiac rhythms and diagnosing heart failure [4–6]. Many other conditions such as hypertension [7], diabetes [8], and neuromuscular diseases [9] can also cause variations in features related to the QRS complex. Therefore, the precise detection of the QRS complex is crucial for guiding clinical decisions pertaining to related illnesses.

Manual QRS detection is time-consuming and prone to subjective errors. Consequently, automated QRS detection algorithms have

* Corresponding author. Department of Bioengineering, Graduate School of Engineering, The University of Tokyo, Tokyo, 113-8656, Japan.

** Corresponding author. Department of Electrical Engineering and Information Systems, Graduate School of Engineering, The University of Tokyo, Tokyo, 113-8656, Japan.

E-mail addresses: zhuozshi@ucla.edu (Z. Shi), tabata@bioeng.t.u-tokyo.ac.jp (H. Tabata).

¹ These authors contributed to the work equally and should be regarded as co-first authors.

<https://doi.org/10.1016/j.heliyon.2024.e28903>

Received 15 January 2024; Received in revised form 22 March 2024; Accepted 26 March 2024

Available online 30 March 2024

2405-8440/© 2024 The Authors. Published by Elsevier Ltd. This is an open access article under the CC BY-NC-ND license (<http://creativecommons.org/licenses/by-nc-nd/4.0/>).

gained prominence, revolutionizing cardiac signal analysis. In recent decades, advancements in QRS detection algorithms have led to two primary categories: traditional signal enhancement methods, and artificial neural networks. Traditional signal enhancement methods rely on well-established signal processing techniques to preprocess ECG data before QRS detection. These techniques involve filters [10], wavelet transforms [11], and empirical mode decomposition [12] are used for denoising. Then, thresholding [13] and morphological operations [14] are used to isolate and enhance the QRS complex. Traditional signal enhancement methods often involve transparent processes, making it easier to understand how the algorithm works. However, they rely heavily on manual feature extraction and handcrafted rules, which may not cover all variations in ECG signals. Artificial neural network-based approaches leverage machine learning models, particularly deep learning architectures like convolutional neural networks (CNNs) [15,16] and recurrent neural networks [15,17], to automatically learn features and patterns from raw ECG data. They often exhibit superior performance, particularly in complex ECG datasets, owing to their ability to learn intricate patterns. Nevertheless, ECG signals are susceptible to various types of noise in real-world measurement conditions. Although artificial neural networks are generally considered to have better noise robustness than traditional methods, their performance inevitably declines with an increase in noise intensity [18,19].

To enhance the robustness of neural network-based QRS detection, we propose a simulated degeneration unit (SDU), which we integrated with a CNN-based QRS detector. The inspiration behind the SDU comes from the degeneration process of interfering optical pulses, where noise energy is utilized to drive the system toward its ground state [20–22]. Compared with traditional filters and signal decomposition methods, SDU can more effectively suppress in-band noise that overlaps with the ECG spectrum. Through performance comparisons with other recently reported methods on three open-source databases, the proposed approach demonstrated state-of-the-art performance for QRS complex detection. Furthermore, testing with several real-world noise injections into ECG signals showed that the utilization of the SDU significantly enhances the robustness of CNN-based QRS detection. The primary contributions of this study are listed below:

- (1) The introduction of the SDU as an additional nonlinear module results in improved QRS detection performance.
- (2) For open-source test databases, the proposed SDU-assisted CNN-based QRS detector exhibits comparable performance to state-of-the-art QRS detectors when no additional noise is injected.
- (3) Under real-world noise stress testing, the noise robustness for achieving optimal performance in the SDU-assisted CNN is enhanced by 167%–300% compared to the CNN without SDU.

For the remainder of this paper, the structure is outlined in the following manner. The SDU mechanism is described in Section 2. Then, the neural network configurations for feature extraction and QRS determination are provided, followed by information on the three testing databases. Sections 3 and 4 present results and discussion, respectively. Finally, Section 5 presents the conclusion of this study.

2. Methodology

2.1. Overall process of the proposed QRS detector

Fig. 1 illustrates the proposed QRS detection process based on SDU. Functionally, the entire process can be divided into three parts. First, the bandpass filter and SDU perform signal enhancement to counteract the adverse effects of excessive noise. Subsequently, the enhanced ECG signal is transformed into signals with different granularity characteristics via the difference and average difference modules. Finally, two types of CNNs extract the features of the preprocessed ECG with different granularities, followed by multilayer perceptron (MLP)-based position determination of the QRS complex.

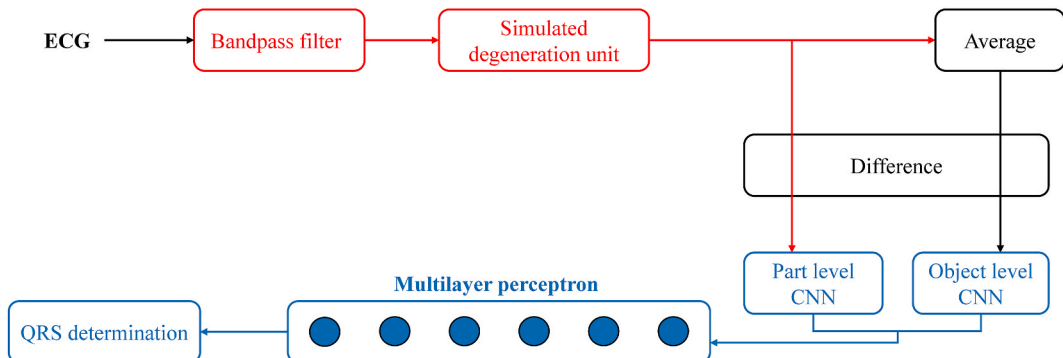


Fig. 1. Overall process of the proposed SDU-assisted CNN-based QRS detector.

2.2. Signal enhancement based on SDU

To eliminate out-of-band noise in the recorded ECG, a bandpass filter is initially employed with cutoff frequencies of 0.05 and 100 Hz. Subsequently, to mitigate in-band noise and enhance the signal-to-noise ratio, the SDU module further processes the ECG signal. The construction of the SDU is inspired by the degeneration dynamics of the degenerate optical parametric oscillator (DOPO), whose physical configuration is depicted in Fig. 2. The heart of a DOPO is a nonlinear crystal, typically made of a material such as periodically poled lithium niobate (PPLN). This material exhibits a nonlinear optical response, indicating that it can interact with photons in such a way that new photons are generated. Inside the crystal, the intense pump beam interacts with the nonlinear medium, leading to the generation of two lower-energy photons, called signal and idler photons. The signal and idler photons are trapped within a ring cavity, which allows for the amplification of the signal and idler photons. Some of the generated photons escape the cavity through an output coupler, providing dynamic information regarding the DOPO. Based on the output information, the injection coupler in the external electronic circuitry can inject the desired input into the ring cavity in the form of feedback pulses.

Because of the phase-sensitive nature, the phase of the modes output from DOPO will find one of the two degenerate phases, 0 or π . Its physical evolution process can be divided into four steps, as depicted in Fig. 3. Initially, because all pulses in the DOPO are uncorrelated, all spin eigenstates possess similar occurrence probabilities [Fig. 3(a)]. Subsequently, under the influence of external driving, the probabilities of the two degenerate ground states increase, while those of the other states are suppressed [Fig. 3(b)]. Subsequently, spontaneous symmetry breaking occurs owing to noise, resulting in one of the two degenerate states obtaining the maximum probability amplitude [Fig. 3(c)]. Finally, because of the quantum-to-classical crossover effect, the observed eigenstate at the macroscopic level is determined as one of the two degenerate states [Fig. 3(d)].

The pulse dynamics within the DOPO can be described by the following c-number stochastic differential equations [23]:

$$\frac{dc}{dt} = (-1 + \rho - c^2 - s^2)c + \frac{1}{A_s} \sqrt{c^2 + s^2} + \frac{1}{2} \frac{d\xi}{dt}, \quad (1)$$

$$\frac{ds}{dt} = (-1 + \rho - c^2 - s^2)s + \frac{1}{A_s} \sqrt{c^2 + s^2} + \frac{1}{2} \frac{d\xi}{dt}, \quad (2)$$

where A_s and $d\xi/dt$ are the saturation amplitude and external injected noise, respectively. The in-phase and quadrature-phase pulse amplitudes during the degenerate process are denoted by c and s , respectively. ρ controls the pumping rate in the DOPO. In a real DOPO, s is much smaller than c and multiplicative noise can be approximately considered as additive noise [24]. Therefore, in the proposed SDU algorithm, Eqs. (1) and (2) can be simplified as:

$$\frac{dc}{dt} = (-1 + \rho - c^2)c + E + \frac{d\xi}{dt}, \quad (3)$$

where E is the input signal. c can be regarded as the output of the SDU, while $\frac{d\xi}{dt}$ can be regarded as the noise contained in the input signal. The solution of Eq. (3) does not rely on analytical methods; instead, it requires numerical methods [25]. In this study, we employed the following fourth-order Runge-Kutta algorithm to solve Eq. (3):

$$q_1 = h((-1 + \rho - c(n)^2)c(n) + E(n)) + \sqrt{h}\xi(n), \quad (4)$$

$$q_2 = h\left(\left(-1 + \rho - \left(c(n) + \frac{k_1}{2}\right)^2\right)\left(c(n) + \frac{k_1}{2}\right) + E(n)\right) + \sqrt{h}\xi(n), \quad (5)$$

$$q_3 = h\left(\left(-1 + \rho - \left(c(n) + \frac{k_2}{2}\right)^2\right)\left(c(n) + \frac{k_2}{2}\right) + E(n+1)\right) + \sqrt{h}\xi(n+1), \quad (6)$$

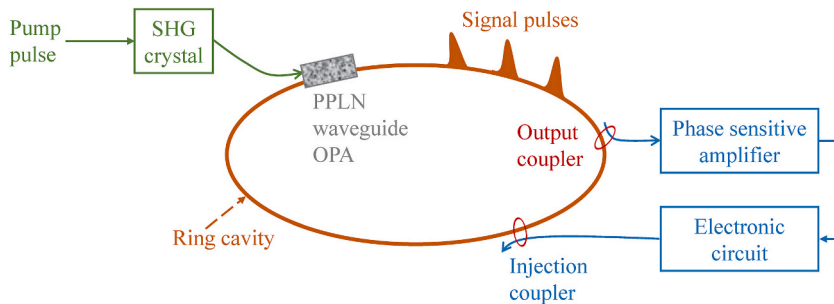


Fig. 2. Configuration diagram of a degenerate optical parametric oscillator (DOPO) achieved through delay fiber loop for optical coupling. SHG: second harmonic generation. OPA: optical parametric amplifier.

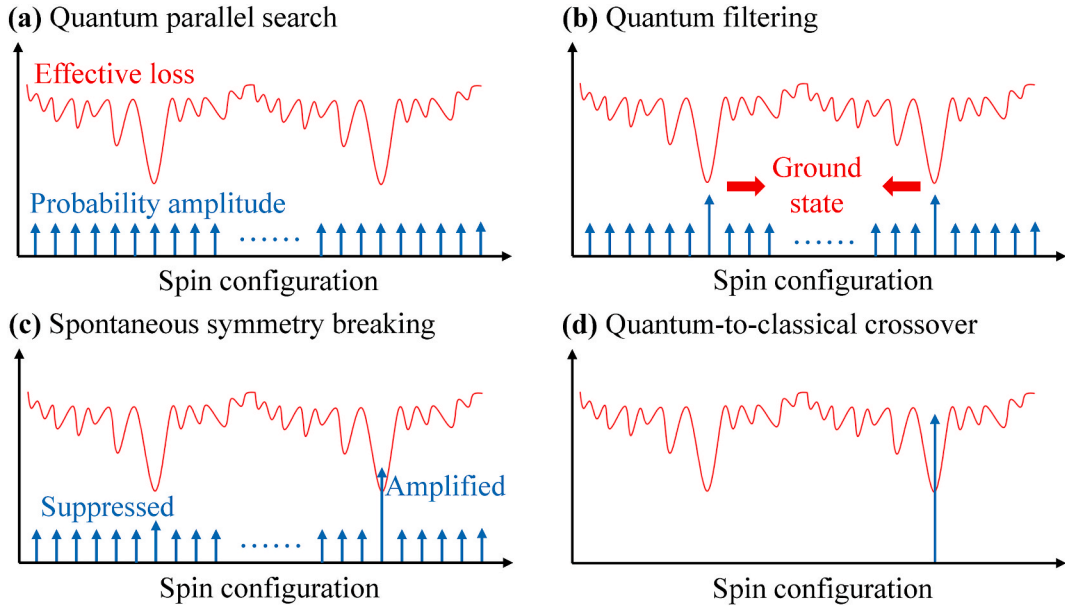


Fig. 3. Degeneration dynamics process of the DOPO: (a) parallel search, (b) filtering, (c) spontaneous symmetry breaking, and (d) crossover effect.

$$q_4 = h((-1 + \rho - (c(n) + k_3)^2)(c(n) + k_3) + E(n + 1)) + \sqrt{h}\xi(n + 1), \tag{7}$$

$$c(n + 1) = c(n) + \frac{1}{6}(q_1 + 2q_2 + 2q_3 + q_4), \tag{8}$$

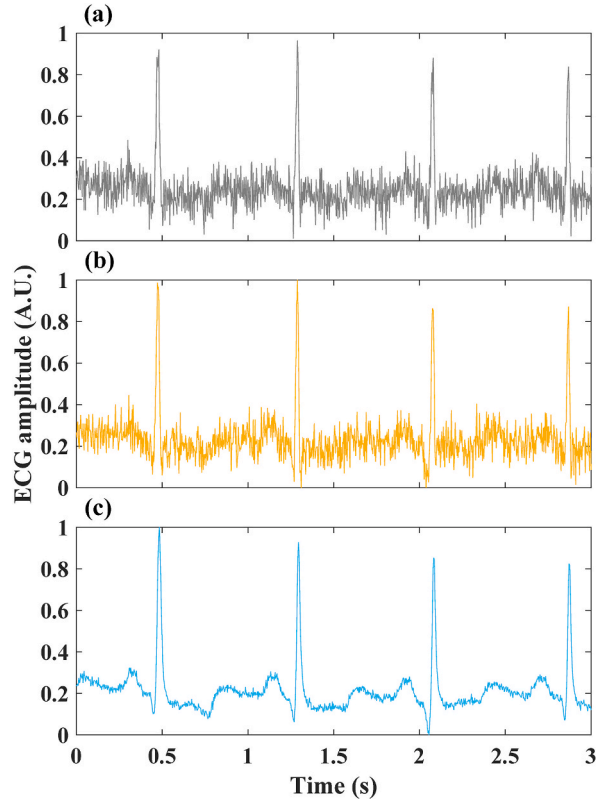


Fig. 4. Waveform examples of (a) noisy ECG, (b) bandpass filtered ECG, and (c) SDU processed ECG.

where n in Eqs. (4)–(8) represents the n -th sampling point. Computational step size h controls the truncation error.

For QRS detection, the input E can be regarded as the ECG signal after processing by bandpass filter. During the training process of the proposed QRS detection algorithm, the parameter ρ in Eq. (3) can be adjusted. To achieve good performance, the optimization of ρ and h is carried out by the open-source automatic optimizer Optuna in Python [26]. The goal of this optimization process is the same as that of the subsequent CNN part.

Fig. 4 illustrates the waveform changes during the signal enhancement stage for a noisy ECG output. In the ECG waveform depicted in Fig. 4 (a), the details are obscured by noise. Although the bandpass filter can eliminate out-of-band noise, it fails to provide comprehensive improvements across the entire frequency spectrum, as shown in Fig. 4 (b). In contrast, following the SDU unit, noticeable noise suppression in the ECG signal is observed, as depicted in Fig. 4 (c). This can be attributed to the partial dissipation of noise energy through the quantum filtering process and spontaneous symmetry breaking in the simulated degeneration dynamics, which effectively enhances the signal-to-noise ratio [23].

2.3. Preprocessing of enhanced ECG

To enrich the features extracted by the CNN, several preprocessing steps are required to obtain two different signals with low amplitudes that carry distinct informative content. The first type of signal is obtained using the following Eq. (9):

$$c_D[n] = c[n+1] - c[n], \quad (9)$$

where c_D is the difference signal, as depicted in Fig. 5(a).

Additionally, sequentially passing the ECG signal output from the SDU through the averaging and difference modules can provide a second type of signal for input into the CNN. These processes are described by the following Eqs. (10) and (11):

$$c_A[n] = \frac{1}{N_i} \sum_{i=1}^{N_i} c[nN + i], \quad (10)$$

$$c_{AD}[n] = c_A[n+1] - c_A[n], \quad (11)$$

where c_A and c_{AD} are the average and average difference signal, respectively. N_i represents the average number, which was set to 5 in this work. Because of the averaging operation, the random noise in c_A and c_{AD} is further attenuated compared with that in c_D , as

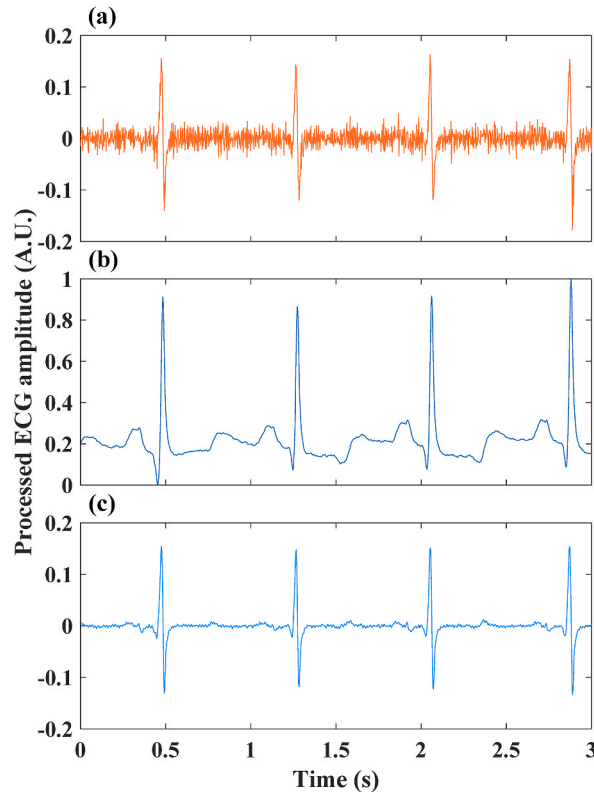


Fig. 5. Waveform examples of SDU processed ECG undergoing (a) difference, (b) average, and (c) average difference operations.

depicted in Fig. 5(b) and (c).

2.4. Feature extraction and QRS position determination

To obtain one-dimensional signal segments for input into the CNN, a sliding detection window should be applied to the pre-processed ECG. For the signal after the differencing operation, a fine-grained segment is extracted by combining the preceding 22 samples and subsequent 33 samples around the current detection point, which serves as the center. After the averaging and differencing operations, the signal is resampled within a window comprising 280 sampling points to acquire coarse-grained segments that match the length of the fine-grained segments. As shown in Fig. 6, fine- and coarse-grained segments are input into two one-dimensional CNNs with different depths. As described in Section 2.1, part-level and object-level CNNs are utilized for feature extraction on c_D and c_{AD} , respectively. Extracting features at different levels of the target signal using CNNs with varying depths is an effective structure that has been widely applied and is also the approach we adopted in this work [27–29]. Table 1 presents the specific parameter configurations for both types of CNN.

Within each layer of the CNN, the convolutional layer performs convolutional computations on the input using shared weights to obtain feature maps. Subsequent downsampling combines the computed results of clustered neurons using average downsampling and outputs them to the next stage. The computation process for the output of the k -th neuron at the l -th layer of the CNN can be described by the following Eqs. (12) and (13):

$$a_k^l = F \left(\sum_{i=1}^{N_{l-1}} 1Dconv(w_{ki}^{l-1}, s_i^{l-1}) + b_k^l \right), \quad (12)$$

$$s_k^l = 1Ddowns(a_k^l), \quad (13)$$

where w_{ki}^{l-1} is the one-dimensional weight kernel connecting the k -th neuron at the l -th layer and i -th neuron at the $(l-1)$ -th layer. s_i^{l-1} is the down-sampled result of the i -th neuron at the $(l-1)$ -th layer. a_k^l and b_k^l denote the convolutional output and bias of k -th neuron at the l -th layer, respectively. The rectified linear unit is selected as the activation function represented by $F()$. Next, the MLP receives all the features s_k^l extracted by the CNN, which can be mathematically described as the following Eq. (14):

$$s_j^m = F \left(\sum_{k=1}^{N_l} w_{jk}^l s_k^l + b_j^m \right). \quad (14)$$

The first layer of the MLP comprises 20 neurons, while the second layer comprises 4 neurons. To distinguish between QRS complexes and non-QRS segments, the output layer of the MLP employs the Softmax function for probability discrimination. During the training process, the backpropagation algorithm is utilized to adjust the weights and biases, and its update rules are as follows:

$$w_{ki}^l(t) = w_{ki}^l(t-1) - \eta \frac{\partial B}{\partial w_{ki}^l(t-1)}, \quad (15)$$

$$b_k^l(t) = b_k^l(t-1) - \eta \frac{\partial B}{\partial b_k^l(t-1)}, \quad (16)$$

where $B = \sum_{j=1}^N (y_{true,j} - y_{pred,j})^2$ in Eqs. (15) and (16) is the objective function which describes the deviation between the true output $y_{true,j}$ and predicted output $y_{pred,j}$. η denotes the learning rate, which is firstly set as 0.005 and gradually decreased by 0.0001% during each learning iteration. The optimizer used for the CNN training process is selected as ADAM.

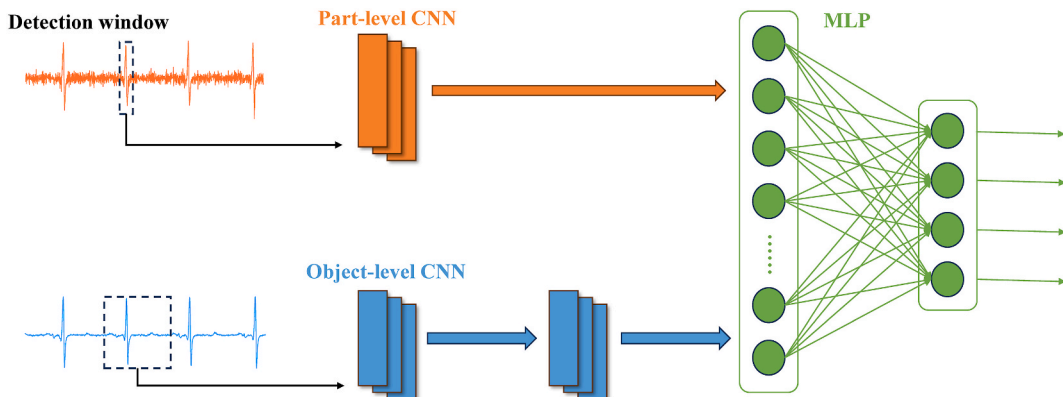


Fig. 6. Structure of one-dimensional CNN for feature extraction and MLP for QRS position determination.

Table 1
Configuration details of two CNNs.

		Part-level CNN	Object-level CNN
CNN layer 1	Convolution kernel length	5	5
	Downsampling factor	2	2
	Neuron number	5	5
CNN layer 2	Convolution kernel length	–	5
	Downsampling factor	–	2
	Neuron number	–	5

2.5. Databases for testing

In this study, three widely used open-source ECG databases, i.e., MIT-BIH Arrhythmia [30], European ST-T (EDB) [31], and MIT-BIH Noise Stress Test (NST) [32] databases were adopted to benchmark the performance of our proposed QRS detection method. The related database details are given in Table 2. For each database, 5-fold randomized cross-validation were adopted for performance testing. Notably, the ECG signals in the EDB database should be upsampled to 360 Hz to ensure uniformity in the sampling frequency across the three databases.

2.6. Noise robustness testing and evaluation approach

In the selected databases, the primary source of noise in the ECG stemmed mainly from the noise inherent in the acquisition process. However, in real-world scenarios, the noise conditions may be worse than those in the test datasets due to variations in the measurement environments and equipment. To assess the robustness of the algorithm, it is necessary to evaluate the performance of our proposed method under the condition of additional injected noise. Additional noise injection is described by the following equation:

$$E_{raw}^i(t) = E_{raw}(t) + D * noise(t), \quad (17)$$

where $E_{raw}(t)$ in Eq. (17) is the original ECG signal obtained from the testing database. $noise(t)$ and D are the injected noise and its noise intensity, respectively. In this study, the injected noise comprised three of the most commonly encountered noises in real-world ECG measurements, namely baseline drift noise (BDN), electrode motion noise (EMN) within the 0–20 Hz range, and muscle noise (MN) within the 20–50 Hz range. These noise profiles can be found in the MIT-BIH NST database.

For detection tasks, sensitivity and precision are usually regarded as the most important performance metrics [33,34]. Therefore, the following three metrics obtained by the following Eqs. 18–20 were used as primary performance evaluation metrics in this study:

$$Sensitivity = \frac{TP}{TP + FN}, \quad (18)$$

$$Precision = \frac{TP}{TP + FP}, \quad (19)$$

$$F1-score = \frac{2 * Sensitivity * Precision}{Sensitivity + Precision}, \quad (20)$$

where TP denotes true positive. FP and FN represent false positive and false negative, respectively.

3. Results

3.1. Test on three databases

Tables 3–5 present the performance of the proposed algorithm on the MIT-BIH arrhythmia, EDB, and MIT-BIH NST databases, respectively. It is evident that, compared to the CNN without SDU, the SDU-assisted CNN significantly reduces both FP and FN in QRS complex detection. Taking the MIT-BIH arrhythmia database as an example, Fig. 7 illustrates some instances of error detection in record 203. In Fig. 7(a), at the annotation of the second QRS complex, there is an atypical waveform. This atypical morphology, which may be caused by premature ventricular contractions, leads to erroneous detections by the CNN both with and without SDU, resulting

Table 2
Details of the three open-source ECG databases used for testing.

Database	# of subjects	Sampling frequency (Hz)	Total beats for testing
MIT-BIH Arrhythmia	48	360	109494
EDB	90	250	788050
MIT-BIH NST	12	360	25590

Table 3
Detector performance on the MIT-BIH arrhythmia database.

QRS detection method	Total beats	TP	FP	FN
CNN without SDU	109494	109090	240	404
SDU-assisted CNN	109494	109330	55	164

Table 4
Detector performance on the EDB database.

QRS detection method	Total beats	TP	FP	FN
CNN without SDU	788050	786036	2987	2041
SDU-assisted CNN	788050	787736	867	314

Table 5
Detector performance on the MIT-BIH NST database.

QRS detection method	Total beats	TP	FP	FN
CNN without SDU	25590	25109	594	481
SDU-assisted CNN	25590	25201	496	389

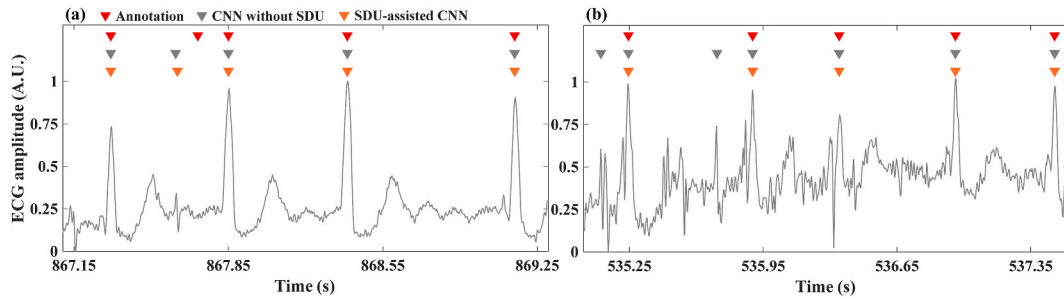


Fig. 7. Incorrect detection instances on record 203 of the MIT-BIH arrhythmia database, including ECG segments with (a) atypical waveforms and (b) heavy noise contamination. The red triangles at the top represent the annotated QRS complex positions in the database. The gray triangles in the middle represent the QRS complex positions detected by the CNN without SDU, while the orange triangles at the bottom represent the positions of the QRS complexes detected by the SDU-assisted CNN. (For interpretation of the references to colour in this figure legend, the reader is referred to the Web version of this article.)

in one FN and one FP. Other cardiac diseases such as left and right bundle branch blocks may also lead to unexpected atypical waveform appearances in ECG, consequently resulting in erroneous detections [35]. Besides the atypical waveform morphology, noise in the record can also affect the performance of the QRS detector. As shown in Fig. 7(b), noise-induced fluctuations cause false detections by the CNN without SDU. In contrast, owing to the attenuation of noise energy, the SDU-assisted CNN generates fewer such false detections.

Table 6
Testing performance of QRS detectors on the MIT-BIH arrhythmia database.

Works	QRS detection method	Sensitivity (%)	Precision (%)	F1-score (%)
Martinez, 2010 [36]	Phasor transform	99.69	99.96	99.82
Merah, 2015 [37]	Stationary wavelet transform	99.84	99.88	99.86
Yakut, 2018 [38]	Pan-Tompkins-based	99.83	99.83	99.83
Burguera, 2019 [10]	Peak-valley detector	99.57	99.37	99.47
Peimankar, 2021 [15]	CNN and Long short-term memory	99.61	99.52	99.57
Rahul, 2021 [13]	Dynamic thresholding	99.82	99.85	99.84
Pander, 2022 [33]	Fuzzy c-median clustering	99.82	99.88	99.85
Lee, 2022 [39]	Empirical mode decomposition	99.83	99.92	99.88
Morshediou, 2023 [40]	Energy operator	99.13	99.41	99.27
Martínez-Suárez, 2024 [41]	Continuous wavelet transform	99.72	99.87	99.80
This work	CNN without SDU	99.63	99.78	99.71
This work	SDU-assisted CNN	99.85	99.95	99.90

3.2. Performance comparison with other QRS detectors

Table 6 presents a comparison of performance metrics between our proposed algorithm and other QRS detectors on the MIT-BIH arrhythmia. When our proposed algorithm operates without the SDU module, the test results for QRS detection show a sensitivity of 99.63%, precision of 99.78%, and F1-score of 99.71%. This performance is only slightly better than that achieved in Refs. [10,15]. In contrast, the utilization of the SDU enhances the performance of the CNN to achieve a sensitivity of 99.85%, precision of 99.95%, and F1-score of 99.90%, surpassing other QRS algorithms.

Table 7 presents a comparison of performance metrics between our proposed algorithm and other QRS detectors on the EDB dataset. Without the SDU module, our proposed CNN achieved test results with a sensitivity of 99.62%, precision of 99.74%, and F1-score of 99.68%. This performance ranks within the mid-range among all compared QRS detection algorithms. However, the SDU-assisted CNN achieved a sensitivity of 99.89%, precision of 99.96%, and F1 score of 99.93%, making it state-of-the-art.

Table 8 illustrates a comparison of performance metrics between our proposed algorithm and other QRS detectors on the MIT-BIH NST dataset. Due to the severe noise pollution present in the MIT-BIH NST database, the performance of the QRS detection algorithm exhibited a noticeable decline compared to the results obtained on the two preceding databases. Without the assistance of the SDU module, our CNN-based QRS detector achieved a sensitivity of 98.12%, precision of 97.69%, and F1 score of 97.91%. In contrast, the use of SDU enhanced the performance of the CNN, achieving a sensitivity of 98.48%, precision of 98.07%, and F1 score of 98.28%. Among all compared algorithms, the SDU-assisted CNN exhibited the best comprehensive performance.

3.3. Noise robustness testing

To quantify the noise robustness, we define the minimum noise intensity, denoted as D_0 , at which the performance of the QRS detector starts to decrease compared to its performance without noise injection. We refer to this as the robustness boundary. Fig. 8(a–c) illustrates the robustness boundaries of the proposed algorithm when injecting different noise levels across the MIT-BIH arrhythmia, EDB, and MIT-BIH NST databases, respectively. When the injected noise is BDN, the use of SDU can increase the robustness boundary of the CNN by 0.3–0.4. For EMN, the SDU-assisted CNN exhibited a robustness boundary only 0.2 to 0.3 higher than that of the CNN without SDU. Regarding MN noise, the SDU can aid the CNN in improving the robustness boundary by 0.2–0.4. When these three noises are mixed, the SDU-induced enhancement in the noise robustness of the CNN-based QRS detector does not surpass the increment observed when injecting pure EMN. Overall, it was demonstrated that the SDU-assisted CNN can maintain its optimal QRS detection performance in an environment with a higher noise level than the CNN without SDU.

3.4. Computational time

Our testing platform is a notebook computer equipped with an RTX 1050 GPU with 6 GB of memory. The computer system has a memory capacity of 16 GB, and the algorithm is configured to undergo training using Python. On the above platform, the average processing time for detecting a 1-min ECG segment is approximately 0.225 s, with 0.025 s attributed to SDU computations. Despite the additional processing time introduced by the inclusion of the SDU, the increased computational overhead is not substantial. Compared to several other algorithms [45,46], our proposed method maintains a computational speed advantage even when utilizing the SDU.

4. Discussion

Based on various performance metrics, the outcomes of this study demonstrate the exceptional performance and noise robustness of the proposed SDU-assisted CNN in QRS detection. The improvement in system performance may be attributed to the nonlinear dynamics of the SDU in the processing of ECG data, which is akin to introducing a nonlinear mapping step. In neural networks, the inclusion of nonlinearity is preferred and usually contributes to enhancing network performance [47]. In addition, the ability of the SDU to dissipate noise energy through simulated degradation dynamics significantly enhances the noise robustness of the CNN. Because these advantages of the SDU are independent of the CNN, this implies that combining the SDU with other neural network architectures also has the potential to enhance QRS detection performance and noise robustness.

Notably, our research has certain limitations in the optimization process of the algorithm. First, in comparison with the parameters that require optimization in the CNN parts, the SDU module involves the optimization of only two parameters. This implies that integrating the optimization of the SDU parameters with those of the CNN into a single optimizer could reduce the computational overhead of optimization. Second, among the numerous optimization algorithms available, there is still room for further exploration to identify the most suitable optimization algorithm for our proposed QRS detector. As the primary focus of this work is not the design of optimization algorithms, delving deeper into these related issues in future research endeavors is deemed important.

5. Conclusion

In this study, we proposed an automatic QRS wave detection algorithm based on an SDU-assisted CNN. Performance comparisons with other algorithms on three widely used open-source databases confirmed the state-of-the-art performance of the SDU algorithm. In addition, the proposed algorithm, benefiting from SDU-induced effective attenuation of the excessive noise impact, possesses stronger robustness than the CNN without SDU.

Considering the nonlinear dynamics of the SDU and its capability to attenuate noise, its integration with a CNN also holds potential

Table 7
Testing performance of QRS detectors on the EDB database.

Works	QRS detection method	Sensitivity (%)	Precision (%)	F1-score (%)
Martinez, 2010 [36]	Phasor transform	99.67	99.73	99.70
Burguera, 2019 [10]	Peak-valley detector	99.88	99.98	99.93
Nayak, 2019 [42]	Digital fractional order differentiator and Hilbert transform	99.87	99.86	99.87
Xiong, 2021 [43]	Energy segmentation	99.77	99.65	99.71
Rahul, 2021 [13]	Dynamic thresholding	99.71	99.80	99.76
Pander, 2022 [33]	Fuzzy c-median clustering	99.67	99.86	99.76
Morshedlou, 2023 [39]	Energy operator	98.93	99.12	99.03
Martínez-Suárez, 2024 [41]	Continuous wavelet transform	99.92	99.55	99.74
This work	CNN without SDU	99.62	99.74	99.68
This work	SDU-assisted CNN	99.89	99.96	99.93

Table 8
Testing performance of QRS detectors on the MIT-BIH NST database.

Works	QRS detection method	Sensitivity (%)	Precision (%)	F1-score (%)
Merah, 2015 [37]	Phasor transform	95.3	93.98	94.63
Khamis, 2016 [44]	Smoothing and Peak-valley detector	93.14	86.23	89.55
Rahul, 2021 [13]	Dynamic thresholding	97.58	96.04	96.80
Pander, 2022 [33]	Fuzzy c-median clustering	95.27	94.70	94.98
This work	CNN without SDU	98.12	97.69	97.91
This work	SDU-assisted CNN	98.48	98.07	98.28

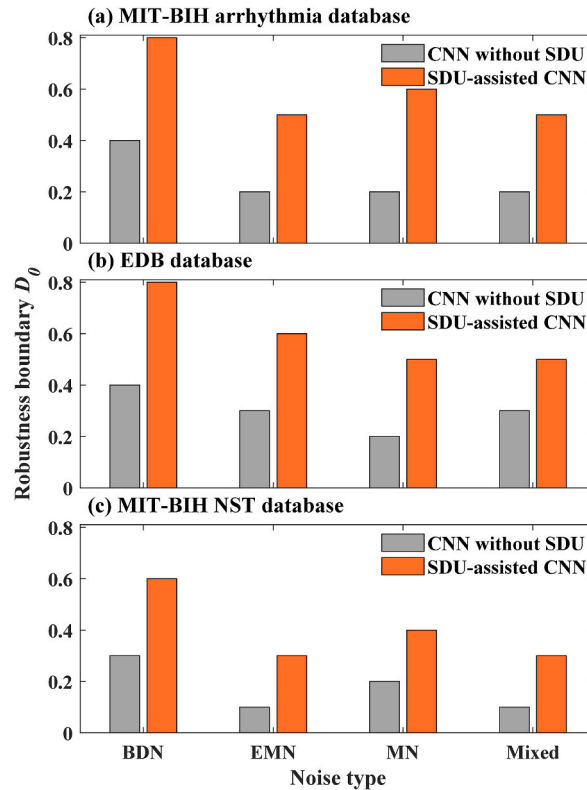


Fig. 8. Robustness boundary D_0 of CNN without SDU and SDU-assisted CNN on (a) MIT-BIH arrhythmia database, (b) EDB database, and (c) MIT-BIH NST database with different additional noise injected.

as a robust intelligent diagnostic system in other clinical scenarios [48–50]. Furthermore, it is worth emphasizing that the dynamic process of the SDU can be implemented not only within algorithms but also in physical systems [23]. This implies that our research could offer valuable insights into the development of hardware systems to support clinical decisions. For instance, physical systems embodying SDU dynamics could be combined with neuromorphic devices [51–53], facilitating faster and more energy-efficient

in-sensor intelligent diagnostics.

Data availability statement

Data associated with this study is available at <https://physionet.org/about/database/>.

CRediT authorship contribution statement

Zhiqiang Liao: Writing – original draft, Visualization, Software, Resources, Methodology, Conceptualization. **Zhuozheng Shi:** Writing – original draft, Validation, Software, Methodology, Conceptualization. **Md Shamim Sarker:** Writing – review & editing, Formal analysis, Data curation. **Hitoshi Tabata:** Writing – review & editing, Supervision, Resources.

Declaration of competing interest

The authors declare that they have no known competing financial interests or personal relationships that could have appeared to influence the work reported in this paper.

Acknowledgements

This research was supported by Institute for AI and Beyond for the University of Tokyo, JST, CREST Grant Number JPMJCR2202, Japan, AMED under Grant Number JP22zf0127006, JSPS KAKENHI Grant Number JP20H05651, JP22K18804, JP23H04099, JP23KJ0605.

References

- [1] M. Yeo, H. Byun, J. Lee, J. Byun, H.Y. Rhee, W. Shin, et al., Robust method for screening sleep apnea with single-lead ECG using deep residual network: evaluation with open database and patch-type wearable device data, *IEEE Journal of Biomedical and Health Informatics* 26 (2022) 5428–5438.
- [2] H.V. Denysyuk, R.J. Pinto, P.M. Silva, R.P. Duarte, F.A. Marinho, L. Pimenta, et al., Algorithms for automated diagnosis of cardiovascular diseases based on ECG data: a comprehensive systematic review, *Heliyon* 9 (2023) e13601.
- [3] X. Wang, X. Han, Z. Chen, Q. Bi, S. Guan, Y. Zou, Multi-scale transition network approaches for nonlinear time series analysis, *Chaos, Solit. Fractals* 159 (2022) 112026.
- [4] C. Liotto, A. Petrillo, S. Santini, G. Toscano, V. Tufano, A multiclass CNN cascade model for the clinical detection support of cardiac arrhythmia based on subject-exclusive ECG dataset, *Biomedical Engineering Letters* 12 (2022) 433–444.
- [5] N. Sabor, G. Gendy, H. Mohammed, G. Wang, Y. Lian, Robust arrhythmia classification based on QRS detection and a compact 1D-CNN for wearable ECG devices, *IEEE Journal of Biomedical and Health Informatics* 26 (2022) 5918–5929.
- [6] F. De Lio, A. Andreis, G. De Lio, M. Bellettini, S. Pidello, C. Raineri, et al., Cardiac imaging for the prediction of sudden cardiac arrest in patients with heart failure, *Heliyon* 9 (2023) e17710.
- [7] S.H. Kim, K.R. Lim, J.-H. Seo, D.R. Ryu, B.-K. Lee, B.-R. Cho, et al., Higher heart rate variability as a predictor of atrial fibrillation in patients with hypertension, *Sci. Rep.* 12 (2022) 3702.
- [8] Q. Qiu, W. Song, X. Zhou, Z. Yu, M. Wang, H. Hao, et al., Heart rate variability is associated with cerebral small vessel disease in patients with diabetes, *Front. Neurol.* 13 (2022).
- [9] N. Xiong, W. Liu, J. Li, S. Luo, W. Gu, W. Zhu, et al., Subclinical cardiac involvement present as electrocardiographic abnormalities in various neuromuscular diseases, *Heliyon* 9 (2023) e13940.
- [10] A. Burguera, Fast QRS detection and ECG compression based on signal structural analysis, *IEEE Journal of Biomedical and Health Informatics* 23 (2019) 123–131.
- [11] A. Ghaffari, H. Golbayani, M. Ghasemi, A new mathematical based QRS detector using continuous wavelet transform, *Comput. Electr. Eng.* 34 (2008) 81–91.
- [12] R. Abdollahpoor, N. Lotfivand, Fully adaptive denoising of ECG signals using empirical mode decomposition with the modified indirect subtraction and the adaptive window techniques, *Circ. Syst. Signal Process.* 39 (2020) 4021–4046.
- [13] J. Rahul, M. Sora, L.D. Sharma, Dynamic thresholding based efficient QRS complex detection with low computational overhead, *Biomed. Signal Process Control* 67 (2021) 102519.
- [14] P.E. Trahanias, An approach to QRS complex detection using mathematical morphology, *IEEE (Inst. Electr. Electron. Eng.) Trans. Biomed. Eng.* 40 (1993) 201–205.
- [15] A. Peimankar, S. Puthusserypady, DENS-ECG: a deep learning approach for ECG signal delineation, *Expert Syst. Appl.* 165 (2021) 113911.
- [16] M. Jia, F. Li, J. Wu, Z. Chen, Y. Pu, Robust QRS detection using high-resolution wavelet packet decomposition and time-attention convolutional neural network, *IEEE Access* 8 (2020) 16979–16988.
- [17] A. Habib, C. Karmakar, J. Yearwood, Domain agnostic post-processing for QRS detection using recurrent neural network, *IEEE Journal of Biomedical and Health Informatics* 27 (2023) 3748–3759.
- [18] J. Chromik, L. Pirl, J. Beilharz, B. Arnrich, A. Polze, Certainty in QRS detection with artificial neural networks, *Biomed. Signal Process Control* 68 (2021) 102628.
- [19] Y. Xiang, J. Luo, T. Zhu, S. Wang, X. Xiang, J. Meng, ECG-based heartbeat classification using two-level convolutional neural network and RR interval difference, *IEICE Trans. Info Syst.* 101 (2018) 1189–1198.
- [20] K. Takata, A. Marandi, Y. Yamamoto, Quantum correlation in degenerate optical parametric oscillators with mutual injections, *Phys. Rev.* 92 (2015) 043821.
- [21] D. Maruo, S. Utsunomiya, Y. Yamamoto, Truncated Wigner theory of coherent Ising machines based on degenerate optical parametric oscillator network, *Phys. Scripta* 91 (2016) 083010.
- [22] P. Kinsler, P.D. Drummond, Quantum dynamics of the parametric oscillator, *Phys. Rev.* 43 (1991) 6194–6208.
- [23] Y. Haribara, S. Utsunomiya, Y. Yamamoto, Computational principle and performance evaluation of coherent Ising machine based on degenerate optical parametric oscillator network, *Entropy* 18 (2016) 151.
- [24] F. Böhm, G. Verschaffelt, G. Van der Sande, A poor man's coherent Ising machine based on opto-electronic feedback systems for solving optimization problems, *Nat. Commun.* 10 (2019) 3538.
- [25] Z. Shi, Z. Liao, H. Tabata, Enhancing performance of convolutional neural network-based epileptic electroencephalogram diagnosis by asymmetric stochastic resonance, *IEEE Journal of Biomedical and Health Informatics* 27 (2023) 4228–4239.

- [26] Akiba T, Sano S, Yanase T, Ohta T, Koyama M. Optuna: a next-generation hyperparameter optimization framework. *Proceedings of the 25th ACM SIGKDD International Conference on Knowledge Discovery & Data Mining* 2019. p. 2623-2631.
- [27] Xiao T, Xu Y, Yang K, Zhang J, Peng Y, Zhang Z. The application of two-level attention models in deep convolutional neural network for fine-grained image classification. *Proceedings of the IEEE Conference on Computer Vision and Pattern Recognition* 2015. p. 842-850.
- [28] Y. Xiang, Z. Lin, J. Meng, Automatic QRS complex detection using two-level convolutional neural network, *Biomed. Eng. Online* 17 (2018) 13.
- [29] F. Li, D. Yao, M. Jiang, X. Kang, Smoking behavior recognition based on a two-level attention fine-grained model and EfficientDet network, *J. Intell. Fuzzy Syst.* 43 (2022) 5733-5747.
- [30] G.B. Moody, R.G. Mark, The MIT-BIH Arrhythmia Database on CD-ROM and software for use with it, in: *Proceedings Computers in Cardiology* 1990, 1990, pp. 185-188.
- [31] A. Taddei, G. Distante, M. Emdin, P. Pisani, G.B. Moody, C. Zeelenberg, et al., The European ST-T database: standard for evaluating systems for the analysis of ST-T changes in ambulatory electrocardiography, *Eur. Heart J.* 13 (1992) 1164-1172.
- [32] G.B. Moody, W. Muldrow, R.G. Mark, A noise stress test for arrhythmia detectors, *Comput. Cardiol.* 11 (1984) 381-384.
- [33] T. Pander, A new approach to adaptive threshold based method for QRS detection with fuzzy clustering, *Biocybern. Biomed. Eng.* 42 (2022) 404-425.
- [34] F. Mormann, R.G. Andrzejak, C.E. Elger, K. Lehnertz, Seizure prediction: the long and winding road, *Brain* 130 (2006) 314-333.
- [35] Z. Zidelmal, A. Amirou, D. Ould-Abdeslam, A. Moukadem, A. Dieterlen, QRS detection using S-Transform and Shannon energy, *Comput. Methods Progr. Biomed.* 116 (2014) 1-9.
- [36] A. Martínez, R. Alcaraz, J.J. Rieta, Application of the phasor transform for automatic delineation of single-lead ECG fiducial points, *Physiol. Meas.* 31 (2010) 1467.
- [37] M. Merah, T.A. Abdelmalik, B.H. Larbi, R-peaks detection based on stationary wavelet transform, *Comput. Methods Progr. Biomed.* 121 (2015) 149-160.
- [38] Ö. Yakut, E.D. Bolat, An improved QRS complex detection method having low computational load, *Biomed. Signal Process Control* 42 (2018) 230-241.
- [39] M. Lee, J.-H. Lee, A robust fusion algorithm of LBP and IMF with recursive feature elimination-based ECG processing for QRS and arrhythmia detection, *Appl. Intell.* 52 (2022) 939-953.
- [40] F. Morshedlou, A.A. Orouji, N. Ravanshad, An energy-efficient analog circuit for detecting QRS complexes from ECG signal, *Integration* 88 (2023) 390-399.
- [41] F. Martínez-Suárez, C. Alvarado-Serrano, O. Casas, Robust algorithm for the detection and classification of QRS complexes with different morphologies using the continuous spline wavelet transform with automatic scale detection, *Biomedical Physics & Engineering Express* 10 (2024) 025008.
- [42] C. Nayak, S.K. Saha, R. Kar, D. Mandal, An efficient and robust digital fractional order differentiator based ECG pre-processor design for QRS detection, *IEEE Transactions on Biomedical Circuits and Systems* 13 (2019) 682-696.
- [43] H. Xiong, M. Liang, J. Liu, A real-time QRS detection algorithm based on energy segmentation for exercise electrocardiogram, *Circ. Syst. Signal Process.* 40 (2021) 4969-4985.
- [44] H. Khamis, R. Weiss, Y. Xie, C.W. Chang, N.H. Lovell, S.J. Redmond, QRS detection algorithm for telehealth electrocardiogram recordings, *IEEE (Inst. Electr. Electron. Eng.) Trans. Biomed. Eng.* 63 (2016) 1377-1388.
- [45] A. Karimipour, M.R. Homaeinezhad, Real-time electrocardiogram P-QRS-T detection-delineation algorithm based on quality-supported analysis of characteristic templates, *Comput. Biol. Med.* 52 (2014) 153-165.
- [46] K. Mourad, B.R. Fethi, Efficient automatic detection of QRS complexes in ECG signal based on reverse biorthogonal wavelet decomposition and nonlinear filtering, *Measurement* 94 (2016) 663-670.
- [47] M.A. Mercioni, S. Holban, The most used activation functions: classic versus current. 2020 International Conference on Development and Application Systems (DAS), 2020, pp. 141-145.
- [48] Y. Mao, K.X.Q. Tan, A. Seng, P. Wong, S.-A. Toh, A.R. Cook, Stratification of patients with diabetes using continuous glucose monitoring profiles and machine learning, *Health Data Science* 2022 (2022).
- [49] Y. Yan, S. Hong, W. Zhang, H. Li, Artificial intelligence in skin diseases: fulfilling its potentials to meet the real needs in dermatology practice, *Health Data Science* 2022 (2022).
- [50] T. Goel, R. Sharma, M. Tanveer, P.N. Suganthan, K. Maji, R. Pilli, Multimodal neuroimaging based alzheimer's disease diagnosis using evolutionary RVFL classifier, *IEEE Journal of Biomedical and Health Informatics* (2023) 1-9.
- [51] Z. Liao, H. Yamahara, K. Terao, K. Ma, M. Seki, H. Tabata, Short-term memory capacity analysis of Lu₃Fe₄Co_{0.5}Si_{0.5}O₁₂-based spin cluster glass towards reservoir computing, *Sci. Rep.* 13 (2023) 5260.
- [52] Z. Liao, Z. Wang, H. Yamahara, H. Tabata, Low-power-consumption physical reservoir computing model based on overdamped bistable stochastic resonance system, *Neurocomputing* 468 (2022) 137-147.
- [53] G.H. Lee, T.-H. Kim, M.S. Song, J. Park, S. Kim, K. Hong, et al., Effect of weight overlap region on neuromorphic system with memristive synaptic devices, *Chaos, Solit. Fractals* 157 (2022) 111999.